

Model-based control of cardiac alternans on a ring

Alejandro Garzón and Roman O. Grigoriev

School of Physics, Georgia Institute of Technology, Atlanta, Georgia 30332-0430, USA

Flavio H. Fenton

Department of Biomedical Sciences, Cornell University, Ithaca, New York 14853, USA

(Received 6 November 2008; revised manuscript received 11 May 2009; published 25 August 2009)

Cardiac alternans, a beat-to-beat alternation of cardiac electrical dynamics, and ventricular tachycardia, generally associated with a spiral wave of electrical activity, have been identified as frequent precursors of the life-threatening spatiotemporally chaotic electrical state of ventricular fibrillation (VF). Schemes for the elimination of alternans and the stabilization of spiral waves through the injection of weak external currents have been proposed as methods to prevent VF but have not performed at the level required for clinical implementation. In this paper we propose a control method based on linear-quadratic regulator (LQR) control. Unlike most previously proposed approaches, our method incorporates information from the underlying model to increase efficiency. We use a one-dimensional ringlike geometry, with a single control electrode, to compare the performance of our method with that of two other approaches, quasi-instantaneous suppression of unstable modes (QISUM) and time-delay autosynchronization (TDAS). We find that QISUM fails to suppress alternans due to conduction block. Although both TDAS and LQR succeed in suppressing alternans, LQR is able to suppress the alternans faster and using a much weaker control current. Our results highlight the benefits of a model-based control approach despite its inherent complexity compared with nonmodel-based control such as TDAS.

DOI: [10.1103/PhysRevE.80.021932](https://doi.org/10.1103/PhysRevE.80.021932)

PACS number(s): 87.19.Hh

I. INTRODUCTION

Ventricular fibrillation (VF), a state of turbulent electrical activity of the heart, is one of the leading causes of sudden cardiac death [1]. Experimental evidence has established that re-entrant waves underlie the vast majority of these cardiac arrhythmias [2–4]. Although many different mechanisms for the initiation and destabilization of reentrant waves have been postulated theoretically [5–9], it has been difficult to verify experimentally which mechanisms are important during the induction and development of fibrillation [10–14]. One of the mechanisms that has been the subject of much study is electrical alternans [15,16] at the cellular level, a long-short beat-to-beat alternation in action potential duration (APD) that arises at fast pacing rates. At the onset of this bifurcation and in small tissues, all the cells go through the same phase of the sequence, either “short” or “long,” on each beat (known as concordant alternans). At faster rates or in much larger tissues, adjacent tissue regions with opposite phases can develop (discordant alternans) [17–19]. Further increases in the rate can produce conduction block [9,18,20], which often can subsequently develop into reentry and fibrillation [21].

At the scale of the entire heart, cellular alternans is believed to be manifested on the electrocardiogram as QRS and/or T-wave alternans [17,19], although recent evidence suggests this association may not be complete [22]. It has been found that patients exhibiting even small T-wave alternans that is not visually apparent (microvolt T-wave alternans) are at a higher risk of developing ventricular arrhythmias [23], and a number of studies have led to the establishment of T-wave alternans as an important marker of susceptibility to sudden cardiac death [24]. Therefore, it would be desirable to have methods to suppress alternans

when they develop in tissue, before they can evolve to fibrillation.

Several feedback control methods for the suppression of alternans and re-entrant arrhythmias based on the application of external electrical stimuli of small intensity have been proposed as methods for the prevention of VF. As of this time, however, none of these methods are close to the stage of development required for clinical implementation. Historically, the first schemes were based on time-delay autosynchronization (TDAS) control. What makes these methods appealing is the ease of their implementation: the calculation of the timing and intensity of the control current is computationally inexpensive and no knowledge of the laws governing the system dynamics is required. In the context of cardiac tissue, TDAS was originally proposed as a way to suppress alternans by Rappel *et al.* [25]. They investigated models of both one-dimensional (1D) and two-dimensional (2D) tissue and concluded that a grid of control electrodes was necessary to stabilize the normal heart rhythm (nonalternating time-periodic solution). Echebarria and Karma [26] showed that alternans in short (a few cm) open 1D fibers could be suppressed using single-electrode TDAS. Their findings were later verified experimentally by Christini *et al.* [27].

More recently, researchers have turned toward more systematic approaches in which knowledge of the laws governing the system dynamics (in the form of a model) is used in the design of the control protocol. One such approach based on quasi-instantaneous suppression of the linearly unstable modes was proposed by Li and Otani [28] for single cells and by Allexandre and Otani [29] for 2D tissue. A significant limitation of this approach is that it is aimed at systems with only one pair of unstable modes. It is unclear whether (and how) it can be generalized to situations where multiple unstable modes coexist and, as we show in this paper, it tends

to produce conduction block for a 1D model with only one pair of unstable modes.

Dubljevic [30] and Dubljevic *et al.* [31] introduced a control method for 1D fibers based on the amplitude equation formalism [32]. Since the amplitude equation formalism is only valid when the action potential duration varies over distances much larger than the wavelength of the spatially periodic solution, the applicability of this approach to cardiac tissue of realistic dimensions is questionable. A canine Purkinje fiber (which is a few cm long), for instance, cannot fit even a single wavelength. For reference, the shortest wavelength of action potential can be estimated as the product of the minimum APD, 120 ms [33], and the minimum conduction velocity, 200 cm/s [34], or about 24 cm.

To address the limitations of these approaches, we present a method based on linear-quadratic regulator (LQR) control [35,36]. Our main goal in this paper is to compare the performance of different control methods—for a particular model and particular geometry—with the aim of establishing the advantages and disadvantages of model- and nonmodel-based control approaches to the suppression of instabilities of the normal heart rhythm.

We start in Sec. II by describing the ionic model of the tissue and the geometry used in this study. TDAS control is presented in Sec. III. The bifurcation analysis of the model is performed in Sec. IV, with Sec. V devoted to model-based control. Finally, our conclusions are presented in Sec. VI.

II. MODEL EQUATIONS

The focus of this paper is to compare and contrast different control approaches, rather than to study a particular physiological condition. Therefore, we choose the simplest model and geometry. Specifically, we will describe cardiac tissue dynamics using the three-variable Fenton-Karma model [37] in a 1D ring geometry. The evolution equation can be written in compact form as

$$\partial_t \mathbf{z} = D \partial_x^2 \mathbf{z} + F(\mathbf{z}) - \mathbf{y}. \quad (1)$$

The system state $\mathbf{z}(x, t) = [u(x, t), v(x, t), w(x, t)]$ includes the voltage variable u and two gating variables v and w , D is a 3×3 matrix whose only nonzero entry is $D_{11} = 1.171 \times 10^{-3} \text{ cm}^2/\text{ms}$ [38], the nonlinear term $F(\mathbf{z})$ describes the local cell dynamics, and $\mathbf{y} = [j(x, t), 0, 0]$, where $j(x, t)$ is an applied external current density. The ring geometry is accounted for by periodic boundary conditions: $\mathbf{z}(0, t) = \mathbf{z}(L, t)$ for all t , where L is the ring length (circumference). Except where stated otherwise, we use the model parameters from Ref. [39]. (Table 1, column labeled MBR).

We excited action potentials on rings of different lengths by application of a bipolar current. For values of L above the critical value $L_c = 10.03 \text{ cm}$ (to be discussed in more detail in Sec. IV), the action potential approaches asymptotically a traveling-wave solution $\bar{\mathbf{z}}(x, t)$ that propagates on the ring with constant speed c and constant shape $\mathbf{z}_p(x)$,

$$\bar{\mathbf{z}}(x, t) = \mathbf{z}_p(x - ct). \quad (2)$$

This traveling-wave solution has periods L and $T = L/c$ in space and time, respectively, and represents normal heart rhythm.

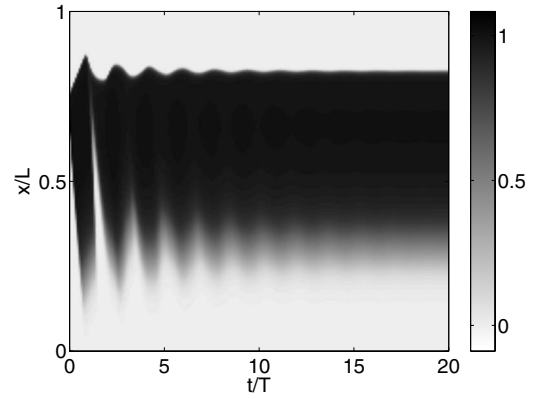


FIG. 1. Evolution of the transmembrane voltage u on a ring of length $L=10.57 \text{ cm}$. Here and everywhere below the spatial position x refers to the *co-moving* reference frame.

The evolution of the action potential is most conveniently represented in a reference frame that moves along the ring with speed c (*co-moving* reference frame). The coordinates in the *co-moving* reference frame (primed) are related to the stationary reference frame coordinates (unprimed) by $x' = (x - ct) \bmod L$. In the *co-moving* frame, after a short transient, the traveling-wave solution (2) becomes stationary for $L > L_c$, as Fig. 1 illustrates. We therefore choose the *co-moving* reference frame to present all our results below.

For $L < L_c$, the system state asymptotically approaches a limit cycle characterized by oscillation of the action potential duration (in the stationary frame) or width (in the *co-moving* frame). An example, as observed in the *co-moving* reference frame, is shown in Fig. 2. This solution, which is time periodic in the *co-moving* reference frame, will appear as quasi-periodic in the stationary reference frame since the frequency with which the pulse propagates around the ring is generally incommensurate with the frequency with which its width oscillates. This is consistent with the results of Courtemanche *et al.* [40] and Comtois and Vinet [41].

In order to quantify the oscillation amplitude, we will define the width of the action potential, $W(t)$, as the length of the *spatial* domain for which the transmembrane voltage u is above some threshold u_{th} . In this work we set $u_{\text{th}} = 0.4$ (see

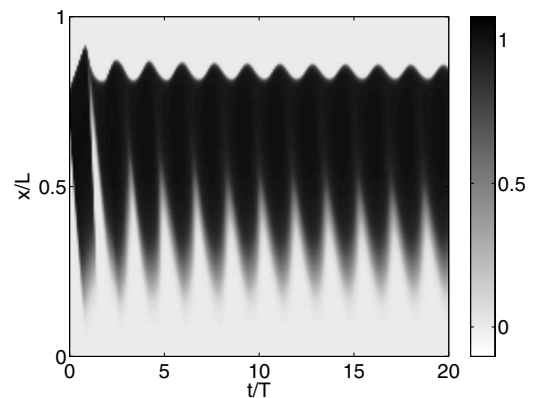


FIG. 2. Evolution of the transmembrane voltage on a ring of length $L=9.94 \text{ cm}$. The asymptotic state corresponds to fully developed alternans.

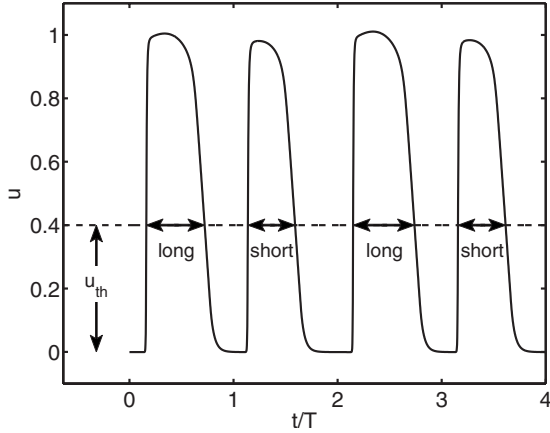


FIG. 3. Transmembrane voltage at a fixed location on a ring of length $L=9.94$ cm. One can see a pattern of alternation between long and short APD, characteristic of alternans.

Fig. 3). For reference, u is defined so that it varies approximately between 0 and 1: $u=(V-V_0)/(V_{fi}-V_0)$ where V is the transmembrane voltage in physical units, $V_0=-85$ mV is the resting membrane voltage and $V_{fi}=+15$ mV is the Nernst potential of the fast inward current. For consistency with this scaling of the voltage, the Fenton-Karma model uses a scaled current-density $j=I/[C_m(V_{fi}-V_0)]$, where I is the current density in physical units and $C_m=1 \mu\text{F}/\text{cm}^2$ is the membrane capacitance.

It should be noted that although the average conduction velocity of the oscillating pulse does depend on the oscillation amplitude (and the ring length), near L_c we find it to coincide to numerical precision with the conduction velocity c of the (unstable) stationary pulse. This can be seen in Fig. 2, where the position of the front of the pulse oscillates, but does not drift, as a function of time.

The observed transition between stationary and oscillatory solutions of the Fenton-Karma model on a ring is qualitatively similar to the transition between normal rhythm and alternans in cardiac tissue. For instance a train of traveling pulses can be created in a Purkinje fiber by pacing it periodically at one end. When the pacing rate is sufficiently low, the pulses propagate without changing shape. If the pacing rate is increased beyond some threshold, the shape oscillates as the pulses travel down the fiber. When the voltage is recorded at a fixed location on the fiber, these oscillations of the pulse shape appear as a beat-to-beat alternation of the APD. For comparison, Fig. 3 represents such a recording for our model. Since the wave speed does not vary significantly, the increase in the pacing rate is equivalent to a decrease in the wavelength. In our model the wavelength is determined by the ring length; therefore, we can identify the limit-cycle oscillation of the pulse width with the state of alternans and the steady state with the normal rhythm.

The ring geometry also can serve as a model for the study of instabilities of reentrant arrhythmias leading to VF. For instance, functional re-entry is often associated with a spiral wave. In Ref. [29], several instabilities producing oscillations of the thickness of the spiral wave (there called ‘‘alternans modes’’) were demonstrated. Away from the tip, each segment of the spiral wave can be thought of as a traveling

wave on a ring. Therefore, although the spiral wave dynamics in 2D is richer, some of the results obtained in the 1D ring geometry might still be of relevance.

Having determined the dynamical regimes, we next turn our attention to the control problem. Specifically, the objective is to suppress the oscillatory dynamics using spatially localized feedback representing current injection through an electrode implanted into the cardiac tissue.

III. NONMODEL-BASED (TDAS) CONTROL

We begin with the TDAS control as implemented in Ref. [25]. To model an experimental setup, we take the current-density $j(x,t)$ to be spatially localized at the position of a single (unipolar) control electrode fixed relative to the tissue at x_0 :

$$j(x,t) = j_0(t)g[s(x-x_0)], \tag{3}$$

where $j_0(t)$ is the control current, $g(s)$ is a normalized Gaussian of width $\sigma \ll L$, and the shift function $s(x)=[(x+L/2)\text{mod } L]-L/2$ takes into account the periodic boundary conditions. In the calculations reported here $\sigma=0.17$ cm.

The control current was calculated in two ways: using bidirectional feedback

$$j_0(t) = \gamma\Delta u(t), \tag{4}$$

and using unidirectional feedback

$$j_0(t) = \gamma\Delta u(t)\Theta[\Delta u(t)], \tag{5}$$

where $\Delta u(t)=u(x_0,t)-u(x_0,t-\tau)$, γ is a tunable parameter, and τ is the time delay calculated as in Ref. [25]. Note that the feedback current is computed based solely on the measurements of the voltage and does not require a model of the dynamics. The TDAS control therefore can be classified as nonmodel-based.

TDAS control was tested by simulating the evolution of the system subject to the feedback law (4) or (5). The evolution Eq. (1) was integrated numerically using the explicit Euler method on a uniform mesh of 2000 points (this amounts to a mesh size of about 5×10^{-3} cm). Finite-differences approximation was used for the diffusion term. The time step was set to 8.25×10^{-4} ms.

It was argued in Ref. [25], that unidirectional feedback (5) effectively restricts the application of the control current to times during which the cells are passing through the repolarization phase of the action potential, eliminating conduction block. This effect was not observed in the model considered here. In particular, the unidirectional feedback (5) produced nonzero control current in both the repolarization and depolarization phases. Furthermore, we found no relation between the phase of the action potential and the sign of Δu . In some cases, while using the bidirectional feedback (4), the sign of Δu alternated from positive to negative from one period to the next in both the depolarization and repolarization phases. This behavior is partially illustrated by Fig. 4 (bottom), which shows the control current calculated via Eq. (4). Notice the alternating sign of the narrow spikes corresponding to the depolarization phase. Also, notice how the small bumps associated with the repolarization phase are initially

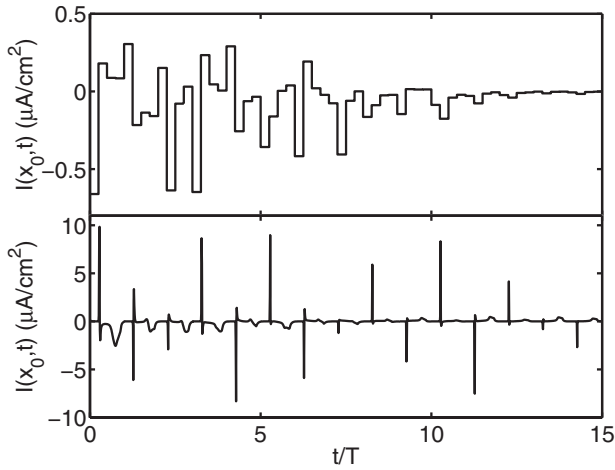


FIG. 4. Control current density at the location of the control electrode $[I(x_0, t)$ as seen in the stationary reference frame] as a function of time for LQR (top) and TDAS (bottom).

negative but become positive in later stages. Bidirectional feedback was generally found to perform better than unidirectional and was therefore chosen for the remainder of this study.

There are many potential reasons why our findings differ from those of the earlier study [25]. Here, only one control electrode is used, while Rappel *et al.* simulated the action of multiple electrodes. Moreover, the earlier study also used different models of cardiac dynamics. Our results suggest that the effect of bi- and unipolar feedback currents on the emergence of conduction block requires further investigation.

To investigate the performance of time-delay feedback control, we investigated the evolution of the system dynamics using the state of fully developed alternans shown in Fig. 2 as an initial condition, with the ring length $L=9.94$ cm. This corresponds to $c=42.3$ cm/s and $T=235$ ms. The evolution of the action potential (for optimal values of x_0 and γ , as explained below) is shown in Fig. 5. The action potential gradually approaches a stationary state with $W(t)=W_0$. Hence, successful suppression of alternans is achieved.

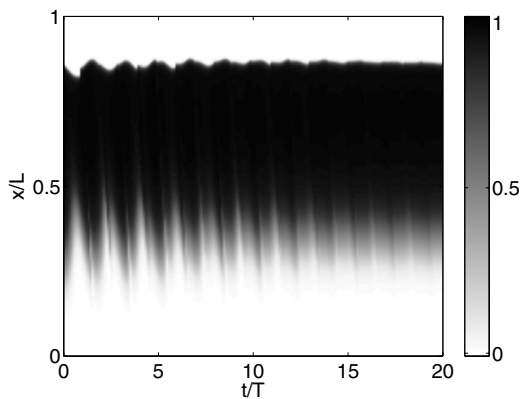


FIG. 5. Evolution of the transmembrane voltage u under TDAS control for the ring of length $L=9.94$ cm. Parameters γ and x_0 were set to the optimal values as described in the text. The initial condition is the state of fully developed alternans shown in Fig. 2.

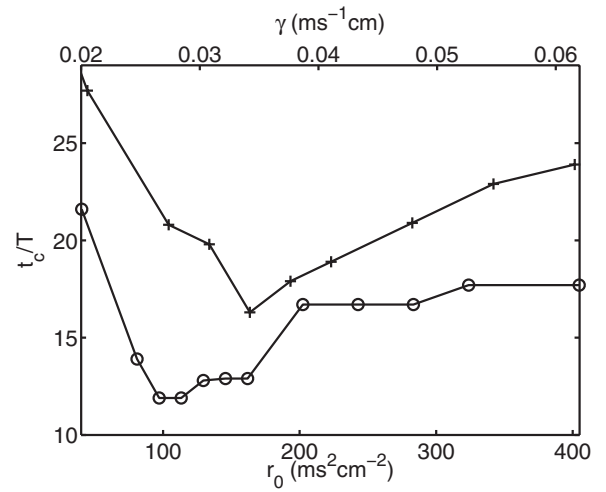


FIG. 6. Control time as a function of control parameters γ for TDAS (crosses) and r_0 for LQR (circles) with $l=4$ subintervals (see Sec. V B).

In order to quantify how quickly alternans is suppressed, we define the control time t_c as the smallest time after control is turned on at $t=0$ for which the absolute value of the variation in the width, $\delta W(t)=W(t)-W_0$, falls below some threshold, δW_{th} , to never go above it again. Here we set $\delta W_{th}=0.05\Delta W$, where ΔW is the maximum value of $|\delta W(t)|$ for the state of fully developed alternans without control. For the value of L used, $\Delta W\approx 0.22W_0$.

Keeping the gain γ fixed at a value of 0.034 ms^{-1} cm, we determined the initial position of the control electrode x_0 giving rise to the lowest value of t_c (this is equivalent to choosing the phase of the oscillation at the instant when the control is turned on). Setting x_0 at that optimal value, we explored the performance of control with different values of γ . As Fig. 6 shows, for TDAS the control time achieves the smallest value $t_c\approx 16.3T=3.83$ s for $\gamma\approx 0.034$ ms^{-1} cm.

As the system approaches the asymptotic state, $\Delta u(t)$ and, as a result, the control current $j_0(t)$ vanishes. This indicates that the asymptotic state is a steady solution (in the absence of control current) of the evolution Eq. (1); i.e., it is the target state (2). In the next section we will show that this state is unstable for $L<L_c$, and hence the dynamics will spontaneously revert to alternans in the absence of control.

IV. BIFURCATION ANALYSIS

The availability of a model allows one to analyze the dynamics and solve the control problem in a systematic, rather than *ad hoc*, way. In particular, the results in Sec. II can be easily understood by performing a linear stability analysis of the traveling-wave state (2). Its stability is easiest to describe in the co-moving reference frame, where the evolution Eq. (1) takes form

$$\partial_t \mathbf{z} = \mathcal{N}[\mathbf{z}] - \mathbf{y}', \quad (6)$$

where

$$N[\mathbf{z}] \equiv c\partial_x \mathbf{z} + D\partial_x^2 \mathbf{z} + F(\mathbf{z}), \quad (7)$$

$\mathbf{y}' = [j'(x', t), 0, 0]$, and $j'(x', t) \equiv j(x' + ct, t)$ is the control current density transformed to the co-moving reference frame. To simplify the notation, we will drop the primes, so that, below, x will refer to the coordinates in the co-moving reference frame.

The traveling wave (2) is a stationary solution of the evolution Eq. (6) in the absence of the control current:

$$N[\mathbf{z}_p] = 0. \quad (8)$$

We calculated \mathbf{z}_p by solving Eq. (8) with periodic boundary conditions using the variational method [42]. The method was modified to obtain a higher density of mesh points in the region where the variables change faster. This allowed the back and the front of the pulse to be accurately resolved while allowing a more sparse sampling of the plateau and the unexcited region.

In order to determine the mechanism leading to the emergence of a limit-cycle oscillation (alternans), we construct the bifurcation diagram for the partial differential Eq. (6). Although bifurcation analysis has been performed previously for single cells, their dynamics are described by ordinary differential equations [43,44], so the results cannot be generalized for the tissue model considered here.

In order to determine which solutions are selected by the dynamics for different ring lengths, we use the linearization

$$\partial_t \delta \mathbf{z} = J_N \delta \mathbf{z} - \mathbf{y}(x, t) \quad (9)$$

of Eq. (6), where $\delta \mathbf{z}(x, t) = \mathbf{z}(x, t) - \mathbf{z}_p(x)$ is the deviation from the stationary state,

$$J_N = c\partial_x + D\partial_x^2 + J_F, \quad (10)$$

and $(J_F)_{ik} \equiv \partial F_i / \partial z_k |_{\mathbf{z}_p}$. In order to avoid the singularity in the elements of J_F introduced by the nondifferentiability at zero of the step functions $f(s) = a\Theta(s) + b\Theta(-s)$ [where $\Theta(s)$ is the Heaviside step function] in the original Fenton-Karma model, their smoothed analogues $f(s) = \alpha + \beta \tanh(s/k)$ were used instead, where $a = \alpha - \beta$, $b = \alpha + \beta$, and $k = 0.03$.

The stability of \mathbf{z}_p is determined by the eigenvalues λ_i of the differential operator J_N ,

$$J_N \mathbf{e}_i(x) = \lambda_i \mathbf{e}_i(x), \quad (11)$$

where $\mathbf{e}_i(x)$ are the corresponding eigenfunctions. The leading eigenvalues and eigenfunctions were found numerically by discretizing Eq. (11) on the mesh used in the variational method. The advection and diffusion terms in J_N were approximated by finite differences. The corresponding matrix eigenvalue problem was then solved via the implicitly restarted Arnoldi iteration method [45] implemented by the MATLAB (Mathworks, Inc.) routine `eigs`.

The real parts of the five leading eigenvalues are shown in Fig. 7 as functions of the ring length L . The trivial eigenvalue, $\lambda_1 = 0$, is independent of the ring length L , with $\mathbf{e}_1 = \partial_x \mathbf{z}_p$. This is a reflection of the translational symmetry of Eq. (6): \mathbf{z}_p remains a stationary solution if shifted by an arbitrary distance. The other four are pairs of complex-conjugate eigenvalues. For $L > L_c \approx 10.03$ cm, all eigenvalues except for λ_1 have a negative real part, such that \mathbf{z}_p is

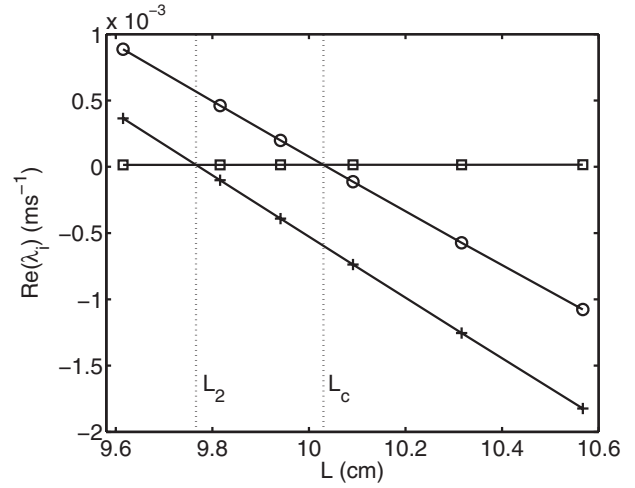


FIG. 7. Real part of the five leading eigenvalues of J_N as a function of the ring length L . Zero eigenvalue λ_1 (squares) is associated with translational symmetry. The first pair of complex-conjugate eigenvalues $\lambda_2 = \lambda_3^*$ (circles) becomes unstable at $L = L_c \approx 10.03$ cm. The second pair of complex-conjugate eigenvalues $\lambda_4 = \lambda_5^*$ (crosses) becomes unstable at $L = L_2 \approx 9.77$ cm.

stable, in agreement with the result presented in Fig. 1. The first complex pair, $\lambda_2 = \lambda_3^*$ acquires a positive real part for $L < L_c$, indicating that a Hopf bifurcation takes place at L_c , giving rise to an oscillatory solution shown in Fig. 2. The target state \mathbf{z}_p becomes linearly unstable, with small perturbations $\delta \mathbf{z}$ growing until the system reaches the state of fully developed alternans with amplitude saturated by nonlinearities.

The amplitude of the alternans, $A_W \equiv \max_t W(t) - \min_t W(t)$, shown in Fig. 8 as a function of L is well fitted by a square-root law $A_W = b|L - L'_c|^{1/2}$ (solid line), characteristic of a supercritical Hopf bifurcation. The fitting parameters were found to be $b = 6.53$ cm^{1/2} and $L'_c = 10.04$ cm using the method of least squares, in agreement (up to the third significant figure) with the value of the critical ring length L_c found via linear stability analysis.

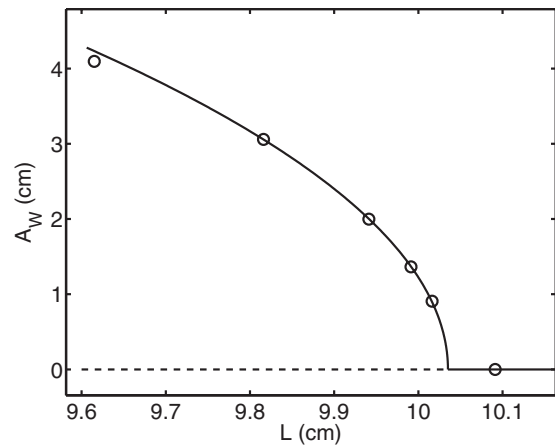


FIG. 8. Amplitude of alternans as a function of the ring length L . The solid curved line is the least-squares fit, $A_W = b|L - L'_c|^{1/2}$, computed using the four middle points. The horizontal solid (dashed) line corresponds to the stable (unstable) steady-state \mathbf{z}_p .

Previous investigations [46,47] discovered that often the state of alternans possesses memory; that is, the alternans produced by an increase in the pacing rate persist even when the rate is subsequently decreased below the threshold at which it was induced. This hysteretic behavior suggests that for a range of pacing rates a stable state of alternans and a stable normal rhythm state coexist (bistability). The *super-critical* Hopf bifurcation found here shows that the Fenton-Karma model on a ring does not possess the memory effect (the latter being consistent with a *subcritical* Hopf bifurcation).

V. MODEL-BASED CONTROL

Now the objective of control can be formulated. Our strategy aims to alter the stability of the target state by applying an external current $j_0(t)$ in such a way that for $L < L_c$ the controlled system will evolve toward \mathbf{z}_p , even when the initial condition corresponds to the state of fully developed alternans.

To facilitate direct comparison, the control current in Eq. (6) is assumed to have the same spatial distribution (3) as that used in TDAS. An electrode fixed with respect to the tissue will appear moving, in the co-moving reference frame, with position given by $x_e \equiv (x_0 - ct) \bmod L$. Therefore, the current density can be written as

$$j'(x', t) = j_0(t)g[s(x' - x_e)]. \quad (12)$$

Although Eq. (9) is an infinite-dimensional system, for L sufficiently near L_c , it possesses a small number of unstable eigenmodes, with stable ones rapidly decaying, so the dynamics of $\delta\mathbf{z}$ can be described reasonably accurately by a Galerkin projection onto the subspace spanned by a finite (in fact, rather small) number of the leading eigenfunctions of J_N . In order to perform this projection we need the eigenfunctions \mathbf{f}_j of the adjoint operator J_N^\dagger ,

$$J_N^\dagger \mathbf{f}_j(x) = \lambda_j^* \mathbf{f}_j(x). \quad (13)$$

With the appropriate normalization, the eigenfunctions \mathbf{f}_j and \mathbf{e}_i satisfy the biorthogonality condition

$$\langle \mathbf{f}_j, \mathbf{e}_i \rangle \equiv \int_0^L \sum_{k=1}^3 f_{j,k}^*(x) e_{i,k}(x) dx = \delta_{ji}, \quad (14)$$

where $\langle \cdot, \cdot \rangle$ denotes the inner product.

The adjoint eigenfunctions \mathbf{f}_j were computed by approximating Eq. (13) by a matrix eigenvalue problem. The matrix representation of J_N^\dagger was obtained by discretizing the equation that defines the adjoint of J_N [48],

$$\langle J_N \mathbf{z}', \mathbf{z}'' \rangle = \langle \mathbf{z}', J_N^\dagger \mathbf{z}'' \rangle, \quad (15)$$

for all \mathbf{z}' and \mathbf{z}'' . From Eq. (15) the matrix elements of J_N^\dagger are found to be related to the matrix elements of J_N by

$$(J_N^\dagger)_{ik} = h_i^{-1} h_k (J_N)_{ki}^*, \quad (16)$$

where h_i is the length of the interval between the mesh points i and $i+1$.

Let ξ_i denote the coefficients in the expansion of $\delta\mathbf{z}$ as a linear combination of the eigenfunctions \mathbf{e}_i ,

$$\delta\mathbf{z}(x, t) = \sum_{i=1}^{\infty} \xi_i(t) \mathbf{e}_i(x). \quad (17)$$

From Eqs. (14) and (17) we find that

$$\dot{\xi}_i(t) = \langle \mathbf{f}_i, \delta\mathbf{z}(t) \rangle. \quad (18)$$

Substituting Eq. (17) into Eq. (9) and applying the operation $\langle \mathbf{f}_j, \cdot \rangle$ to each side of the resulting equation, we obtain

$$\dot{\xi}_j = \lambda_j \xi_j - \langle \mathbf{f}_j, \mathbf{y} \rangle, \quad j = 1, \dots, m, \quad (19)$$

where m is the number of modes considered.

A. Quasi-instantaneous suppression of unstable modes (QISUM)

We start by considering a feedback control method proposed in Refs. [28] and [29] the idea of which is to eliminate the unstable modes by applying a short current stimulus. We should point out that this is essentially a particular implementation of dead beat control [49]. Suppression of alternans using this method was investigated both for single cells and for 2D tissue. In the latter case the target state was a spiral wave that appears stationary when observed in a rotating reference frame. In this sense it is analogous to the traveling-wave solution on the ring considered here.

The effect of a constant control current $j_0(t) = j_0^n$ acting during a brief time interval $[t_n, t_n + \Delta t]$ can be calculated by integrating Eq. (19) over that interval

$$\xi_i(t_n + \Delta t) = \xi_i(t_n) + \lambda_i \int_{t_n}^{t_n + \Delta t} \xi_i(t) dt - j_0^n \int_{t_n}^{t_n + \Delta t} \eta_i(x_0 - ct) dt, \quad (20)$$

where

$$\eta_i(x_0 - ct) = \int_0^L f_{i,1}^*(x) g[s[x - x_e(x_0 - ct)]] dx. \quad (21)$$

Assuming the interval is short enough ($\lambda_i \Delta t \ll 1$ and $c \Delta t \ll a$), Eq. (20) can be approximated by

$$\xi_i(t_n + \Delta t) - \xi_i(t_n) = -j_0^n \Delta t \eta_i(x_0 - ct_n). \quad (22)$$

The method requires the feedback current to be chosen such that

$$\xi_i(t_n + \Delta t) = 0 \quad (23)$$

for all unstable modes i .

It is clear that at most one pair of unstable modes can be eliminated by an appropriate choice of j_0^n . Therefore, the method may only work for ring lengths $L_2 < L < L_c$ (see Fig. 7). Therefore, we set the ring length to be the same as that used previously in TDAS control, $L = 9.94$ cm. For the complex-conjugate unstable modes $\mathbf{e}_2 = \mathbf{e}_3^*$ and $\mathbf{f}_2 = \mathbf{f}_3^*$ (recall that the real mode 1 has a zero growth rate). Since $\delta\mathbf{z}$ is real, we should have $\xi_2 = \xi_3^*$ at all times. Therefore, for the feedback current

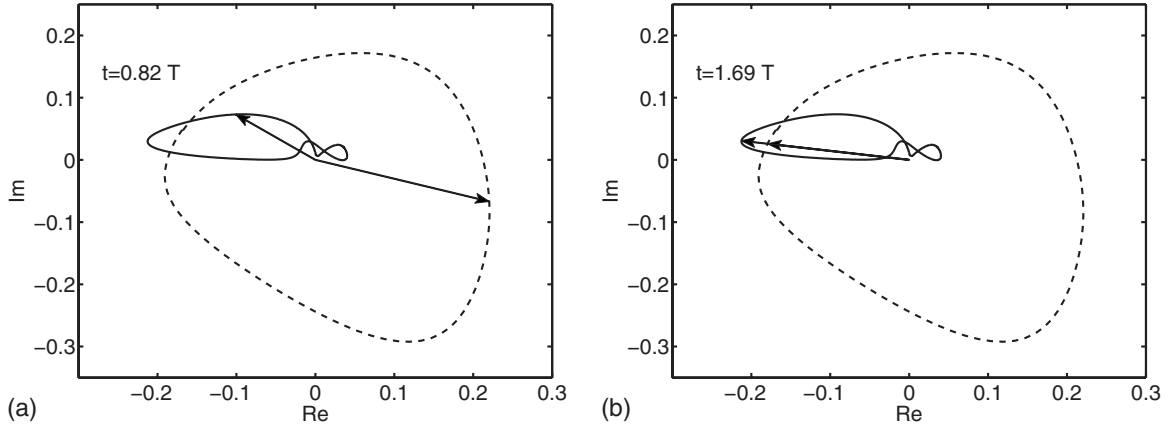


FIG. 9. Trajectories followed in the complex plane by ξ_2 (dashed line) in the state of alternans and η_2 (solid line) over the time interval $[0, T_A]$, where $T_A \approx 1.72T$ is the period of alternans. Arrows are drawn to help identify the angles of ξ_2 and η_2 at a particular time instance. (a) Generically $\phi(x_0, t_0) \bmod \pi \neq 0$. (b) By an appropriate choice of x_0 and t_0 both Eqs. (26) and (27) can be satisfied. Note that η_2 is shown rescaled by a factor of 2 to aid visualization.

$$j_0^n \Delta t = \frac{\xi_2(t_n)}{\eta_2(x_0 - ct_n)} = \frac{|\xi_2(t_n)|}{|\eta_2(x_0 - ct_n)|} e^{i\phi(x_0, t_n)}, \quad (24)$$

where ϕ is the complex phase difference

$$\phi(x, t) = \arg[\xi_2(t)] - \arg[\eta_2(x - ct)], \quad (25)$$

eliminating mode 2 automatically eliminates mode 3 as well. One finds that ξ_2 and η_2 rotate in the complex plane with different angular speeds and in general have different complex phases [see Fig. 9(a)]. Hence, the right-hand side of Eq. (24) is generally complex, while the left-hand side is always real. We must, therefore, choose x_0 and/or t_n such that the right-hand side is real; i.e.,

$$\phi(x_0, t_n) \bmod \pi = 0. \quad (26)$$

Equation (26) has an infinite number of solutions. That freedom can be used to perform some limited optimization [28]. In particular, we find that over one period of the oscillation, $|\xi_2|$ varies much less than $|\eta_2|$. Therefore, for the initial control stimulus, $n=0$, the control current can be minimized by choosing x_0 and t_0 such that $|\eta_2(x_0 - ct_0)|$ achieves its largest value. Since $g(s)$ is a narrow Gaussian ($\sigma \ll L$), $|\eta_2(x)| \approx |f_{2,1}(x)|$. We can, therefore, choose

$$(x_0 - ct_0) \bmod L = x_{\max}, \quad (27)$$

where $x_{\max} \approx 0.8L$ is the location at which $|f_{2,1}|$ achieves its maximum value (see Fig. 10). Similar arguments were used in Ref. [29], to place the current injection aimed at suppressing alternanslike dynamics of a spiral wave. From Eq. (26) we see that t_0 is a solution of $\arg[\xi_2(t_0)] = \arg[\eta_2(x_{\max})] + \pi k$ with some integer k and $x_0 = (x_{\max} + ct_0) \bmod L$. The solution corresponding to $k=0$ is shown in Fig. 9(b). At $t=t_0$ we have $x_e = x_0 - ct_0 = x_{\max}$, which means that it is optimal to apply the control current at the early plateau phase (see Fig. 10). This conclusion is consistent with the results of Ref. [28].

We have investigated the performance of this control algorithm using the initial condition shown in Fig. 2, similar to TDAS. The explicit Euler method becomes unstable for Eq.

(6) due to the presence of the advection term. For that reason, Eq. (6) was integrated using an operator-splitting method. The finite-differences approximation and the Crank-Nicolson method were used for the diffusion and advection terms, while the reaction terms were advanced by Heun's method [50]. A uniform mesh with 2000 points was used. The time step was set to 2×10^{-3} ms.

Fig. 11 shows the evolution of $\xi_2(t)$ leading to and following the initial control stimulus at $t_0 = 0.78T$. The effect of the feedback current was simulated by instantaneously changing $u(x, t_0)$ by $-j_0 \Delta t g\{s[x - x_e(x_0 - ct_0)]\}$ with j_0 computed from Eq. (24), which corresponds to the limit $\Delta t \rightarrow 0$. One discovers that although $\xi_2 = \xi_3 = 0$ (to numerical precision) following the control stimulus, both unstable modes quickly grow to a magnitude comparable to that preceding the current injection. This is due to the so-called control spillover effect [51]: the feedback that is aimed at suppressing the unstable modes will generically excite the modes that would be stable in the absence of feedback (e.g., modes 4, 5, etc.). The nonlinearities contained in the ionic model couple

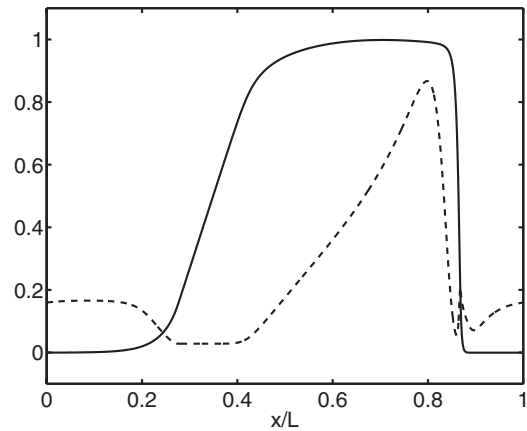


FIG. 10. Transmembrane voltage u of the target state \mathbf{z}_p (solid line) and $|f_{2,1}|$ (dashed line). Notice that the maximum of $|f_{2,1}|$ corresponds to the early part of the action potential plateau following depolarization.

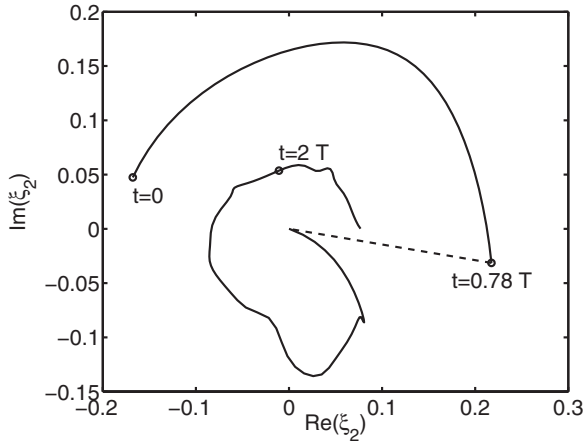


FIG. 11. Trajectory followed by $\xi_2(t)$ in the complex plane before and after the application of a control stimulus $j_0\Delta t$ at $t = 0.87T$. The dashed line indicates the instantaneous cancellation of ξ_2 . The state at $t=0$ is that of fully developed alternans (see Fig. 2).

the dynamics of different modes, leading to a relatively quick regrowth of the unstable modes and re-emergence of the alternans.

One way to address this problem is by iterating the control current injections indefinitely. However, for the application of the second (and subsequent) control stimulus there is no longer the freedom to choose x_0 as it is impractical to move the electrode relative to the tissue. The feedback current should be injected through the electrode located at x_0 at time t_n satisfying Eq. (26). In general we will have $x_e(t_n) = (x_0 - ct_n) \bmod L \neq x_{\max}$ and hence $|\eta_2|$ may be significantly reduced compared to its maximum value. In particular, when the control electrode is located near a minimum of $|f_{2,1}|$ (the extreme case being $x \approx 0.35L$, as Fig. 10 shows) the control current magnitude will have to be increased by two orders of magnitude compared with the optimal choice described previously, with a high likelihood of producing conduction block. This is indeed what we observed. We applied several control stimuli separated by a minimum time of T . This delay was introduced to allow the stable modes to relax following the previous control stimulus. Regardless of the choice of the phase difference (0 or π), conduction block was observed after the application of fewer than 10 control stimuli. Figure 12 shows results obtained for the case in which the shortest interval $|t_n - t_{n-1}|$ between the control stimuli was chosen. Conduction block was observed at $t \approx 14T = 3.29$ s.

B. LQR control

Alternatively, the feedback law could be derived systematically by using a standard control theoretic approach, such as linear-quadratic regulator or LQR. We will limit our focus here to the time-discrete version of LQR. A continuous version of this method is more computationally intensive, but also more efficient.

We start by reducing Eq. (19) to a stroboscopic map that evolves the amplitudes of the leading modes ξ_i in time steps of duration T . On each interval $[t_n, t_{n+1})$, $t_n \equiv nT$, $n = 0, 1, 2, \dots$ we will assume the control current to be piece-

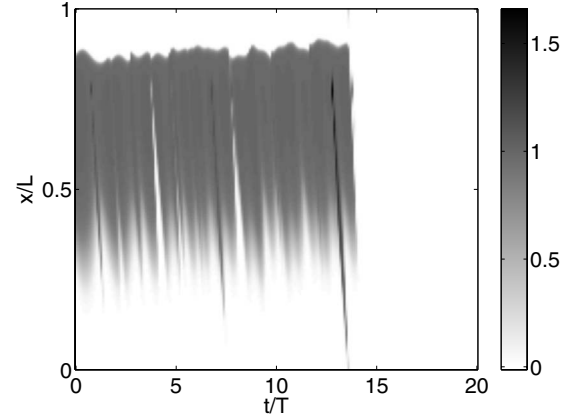


FIG. 12. Evolution of the transmembrane voltage u under QISUM control for the ring of length $L = 9.94$ cm. The initial condition is the state of fully developed alternans shown in Fig. 2. The control method was turned off after the occurrence of conduction block.

wise constant. Specifically, each period of the stroboscopic map will be subdivided into l subintervals $S(n, k) = [t_n + (k-1)\Delta T, t_n + k\Delta T)$, $k = 1, \dots, l$ of equal duration $\Delta T = T/l$, so that

$$j_0(t) = j_0^{n,k}, \quad t \in S(n, k). \quad (28)$$

The stroboscopic map truncated to the m leading modes is obtained by integrating Eq. (19) over the interval $[t_n, t_{n+1}]$ which, taking into account Eqs. (12) and (28), yields

$$\xi^{n+1} = A\xi^n + B_j^n, \quad (29)$$

where $\xi^n = [\xi_1(t_n), \dots, \xi_m(t_n)]$, $j_0^n = [j_0^{n,1}, \dots, j_0^{n,l}]$, A is an $m \times m$ diagonal matrix with elements $A_{ii} = \exp(\lambda_i T)$, and B is an $m \times l$ matrix with elements

$$B_{ik} = -\exp(\lambda_i T) \int_{S(n,k)} \exp(-\lambda_i \tau) \eta_i(x_0 - c\tau) d\tau. \quad (30)$$

LQR control is computed as the solution j_0^n minimizing a quadratic cost function

$$G = \sum_{n=1}^{\infty} [(\xi^n)^\dagger Q \xi^n + (j_0^n)^\dagger R j_0^n], \quad (31)$$

subject to the constraint (29). Q and R are arbitrary positive-definite constant matrices that can be chosen to achieve a particular optimization goal. In particular, setting $Q_{ik} = \langle \mathbf{e}_i, \mathbf{e}_k \rangle / L^2$ and choosing R as a multiple of the $l \times l$ unit matrix reduces Eq. (31) to the form

$$G = \sum_{n=1}^{\infty} \frac{1}{L^2} \|\delta \mathbf{z}(t_n)\|_2^2 + r_0 \sum_{n=1}^{\infty} \frac{1}{l} \sum_{k=1}^l (j_0^{n,k})^2, \quad (32)$$

which respects the translational invariance of the evolution equation in space and time. By varying the scalar parameter r_0 one can obtain the feedback which either minimizes the control current or increases the convergence speed to the target state; r_0 is analogous to the parameter γ of TDAS.

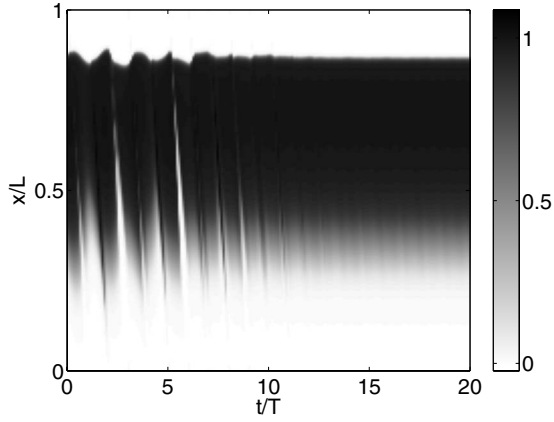


FIG. 13. Evolution of the transmembrane voltage u under LQR control for the ring of length $L=9.94$ cm. We used $l=4$, with r_0 and x_0 set to the optimal values as described in the text. The initial condition is the state of fully developed alternans shown in Fig. 2.

It can be shown [35] that Eq. (31) achieves its minimum when

$$j_0^n = -K\xi^n, \quad (33)$$

where the feedback gain matrix K is related to the solution of a matrix Riccati equation which incorporates matrices A , B , Q , and R . We computed it using the function `dlqr` of MATLAB. Substituting Eq. (33) into Eq. (29), one obtains the closed-loop map

$$\xi^{n+1} = (A - BK)\xi^n, \quad (34)$$

where the matrix $A - BK$ is a stable matrix, so that ξ^n decays to zero, with the system asymptotically approaching the target state \mathbf{z}_p .

The LQR control scheme was verified by numerically integrating the evolution Eq. (6) using the same method, spatial mesh and time step as those used for QISUM control. We found LQR to be capable of quickly suppressing alternans for an appropriate choice of parameters (m , l , x_0 , and r_0). The evolution of the system in the co-moving reference frame is shown in Fig. 13. One finds that the feedback current computed using LQR successfully suppresses fully developed alternans (initial condition shown in Fig. 2) with the system dynamics approaching the target state.

In implementing LQR control we used $m=9$ mode truncation. Increasing m had little effect on the performance. However, we did find that the performance depended noticeably on the position of the control electrode (relative to the position of the traveling pulse at times $t_n=nT$). For some values of x_0 conduction block took place, and the method therefore failed to drive the system to the target state. In the cases in which LQR was successful, the control time was found to depend significantly on the choice x_0 . In the end we selected x_0 to minimize the control time t_c . This value was chosen for all the calculations presented here.

To investigate the constraints on the number of subintervals l , we fixed $r_0=405$ ms² cm⁻² and subdivided each time interval $[t_n, t_{n+1}]$ into $l=2^k$ subintervals with $k=1, \dots, 7$. For $l \leq 2$ the control current was found to produce conduction

block. The control was successful for $l \geq 4$, so we set $l=4$ in the rest of the calculations reported here. This corresponds to the “worst case scenario;” increasing l should further optimize control, thereby decreasing the control time and the control current magnitude and further reducing the likelihood of conduction block.

In order to explore how the LQR control performs depending on the weight given to the magnitude of control current vs. the convergence speed, we computed t_c as a function of r_0 . As Fig. 6 shows, the control time achieves its minimum value of $t_c \approx 11.9T = 2.80$ s for $r_0 \approx 111$ ms² cm⁻² and increases slightly for values of r_0 either greater or less than the optimal value. This time is shorter than that for TDAS. This is the first clear indication that by using more extensive information about the system state and dynamics it is possible to design a control scheme with superior performance.

Fig. 4 shows the control current as a function of time for LQR and TDAS for the values of r_0 and γ producing the smallest t_c . For TDAS the current shows pronounced spikes whose absolute values are about an order of magnitude bigger than the maximum absolute value of the current for LQR. Large currents, such as those applied during the initial stages of control, can lead to electroporation of the tissue surrounding the electrode. Electroporation is characterized by rupture of cell membranes as a result of induced high transmembrane voltage [52,53]. The associated changes in the local dynamics can render any feedback control ineffective.

It should be noted that the convergence of the alternans amplitude $\delta W(t)$ to zero is nonmonotonic, but rather is characterized by strong initial fluctuations. The changes in the action potential shape produced by LQR control during this initial stage (shown in Fig. 14) could be interpreted as induced dispersion of repolarization. For a longer (shorter) pulse, the feedback current repolarizes (depolarizes) the tissue, effectively shortening (lengthening) the pulse.

Observations of uncontrolled cardiac dynamics have found that dispersion of repolarization is a condition that can lead to conduction block [17,20,54]. As we have shown previously, for $l \leq 2$ (when the control current is not allowed to vary sufficiently frequently) LQR does indeed fail by inducing conduction block. However, when the control current profile is sufficiently optimized (for $l \geq 4$), LQR succeeds in suppressing alternans without inducing conduction block. This fact indicates there is no direct link between the alterations of the action potential shape presented in Fig. 14 and conduction block. In other words, the intuition gained in studies of open-loop (uncontrolled) systems cannot be generalized in a straightforward manner to closed-loop (controlled) systems.

C. Robustness of LQR under parameter uncertainty

A source of concern in implementing model-based control is the unavoidable mismatch between the true dynamics and the predictions of the model. A controller that is able to achieve its goal even when this mismatch is present is said to be robust under model uncertainty. The robustness of LQR control can be tested, for instance, by assuming that although

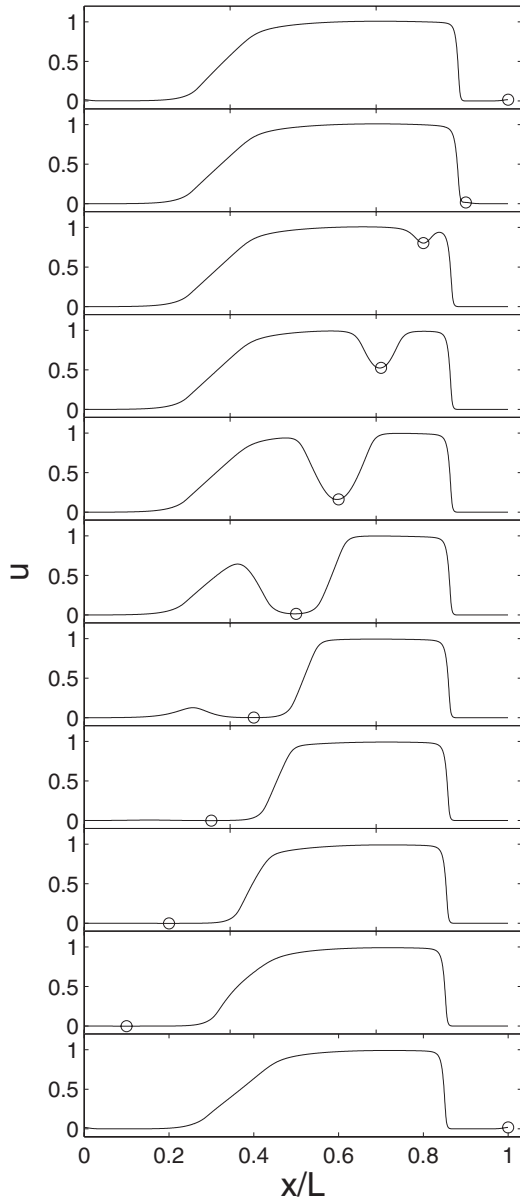


FIG. 14. Transmembrane voltage u during LQR control (same data as for Fig. 13) for t from $5.1T$ (top panel) up to $6.1T$ (bottom panel) with increments of $0.1T$. The circle on each panel indicates the value of u at the location of the control electrode (it moves backward in the co-moving reference frame).

the Fenton-Karma model provides an accurate representation of the real dynamics, the values of its parameters are not known precisely (parameter uncertainty). We tested the performance of LQR in a hypothetical situation in which the “estimated” values of parameters used for computing the feedback were different from the “true” values used to evolve the system state.

In practice the model parameters are estimated by fitting the model predictions to experimental measurements. One of the most easily accessible measurements is the wave speed c of the target state (2). Therefore, we choose the estimated values in such a way that the speed c was the same (up to six significant figures) for the estimated set and the true set of parameters. Specifically, we chose $\tau_r=55.53$ (all times are in

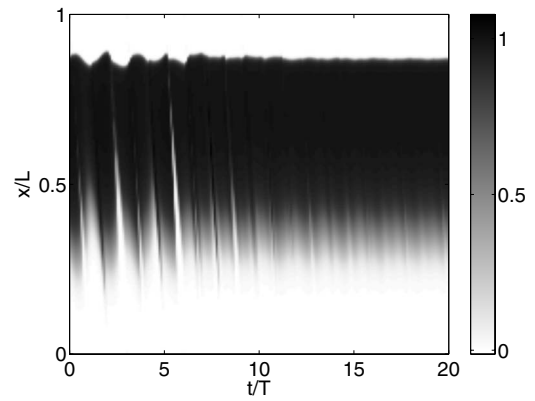


FIG. 15. Evolution of the transmembrane voltage u under LQR control computed using estimated parameters for the ring of length $L=9.94$ cm. Parameters l , r_0 , and x_0 are as in Fig. 13. The initial condition is the state of fully developed alternans (see Fig. 2).

milliseconds) and $\tau_{si}=50$ for the estimated set of values, compared with $\tau_r=50$ and $\tau_{si}=44.84$ for the true set of values, with the rest of the parameters chosen to be the same as in Sec. II. That corresponds to a mismatch of about 10% between the estimated and true values of both parameters.

Fig. 15 illustrates the performance of feedback control computed using the estimated values of parameters. Of course, complete suppression of the perturbation δz cannot be attained, since the target state calculated from the estimated set of parameter values is not the true target state. Nonetheless, after 30 periods control reduces the amplitude of alternans to 5% of the amplitude of fully developed alternans, thereby illustrating that LQR is robust under parameter uncertainty for the model considered.

VI. CONCLUDING REMARKS

This study demonstrates that LQR control considerably outperforms TDAS in suppressing alternans. The advantages of LQR over TDAS are twofold: (i) alternans is suppressed in a shorter time and (ii) the risk of tissue damage is reduced due to a smaller control current. Although we used a particular control theoretic approach (LQR), our results support the conclusion that using knowledge of cardiac dynamics in the implementation and development of control procedures generally allows one to improve the effectiveness, while at the same time reducing the side effects of control, compared with the leading existing approaches such as TDAS. Although our results apply only to a rather simplified situation (the Fenton-Karma model in a 1D medium with periodic boundary conditions), they suggest that model-based control should have similar advantages for actual cardiac tissue. In order to test this hypothesis, more realistic ionic models and physiologically relevant geometries must be investigated first, with experimental validation to follow.

In the conclusion of this paper, it is important to mention another issue that inevitably will arise in an experimental implementation of any model-based control protocol: determining the system state. For instance, LQR requires the knowledge of the complete system state (all the model vari-

ables at all points in space) at the beginning of each time period, $t=t_n$. Although the use of voltage- and calcium-sensitive dyes and microelectrode recordings in principle allows one to determine the spatial distribution of certain model variables in real time [31], this approach is extremely impractical, especially *in vivo*. A more practical alternative approach involves state reconstruction (or state estimation, in the language of control theory) based on measurements of a few model variables at one or several spatial locations [35,36]. In particular, it should be generically possible [55] to reconstruct all dynamical variables required for computing the control current based on measurements of a single variable at a single spatial location. In principle, this can be accomplished, for instance, by recording the transmembrane potential using the same electrode that is used for control. A control scheme based on state estimation will be the subject of a future study.

There is no guarantee that LQR as implemented here will succeed at suppressing alternans in all physiologically relevant ranges of parameters and initial conditions. This is primarily due to the fact that a linear approximation of the

dynamics is used for the calculation of the control current. The occasional failures of this approximation are made evident by the several instances reported here in which LQR control induced conduction block, an essentially nonlinear phenomenon. Similarly, at large amplitudes, the average conduction velocity of the fully developed alternans state might deviate sufficiently from that of the target state for linear control to be successful. Besides shielding the control method against conduction block, incorporating elements of nonlinear dynamics of the system is also expected to improve efficiency as reflected, for example, in a reduction in the control time and the current magnitude. This topic will be addressed in future research.

ACKNOWLEDGMENTS

This work was supported in part by the National Institutes of Health under Grant No. HL075515-S03,-S04 (FHF) and by the National Science Foundation under Grant No. 0800793 (FHF).

-
- [1] W. Rosamond *et al.*, *Circulation* **117**, e25 (2008).
 [2] K. Nanthakumar, J. Jalife, S. Masse, E. Downar, M. Pop, J. Asta, H. Ross, V. Rao, S. Mironov, E. Sevaptsidis *et al.*, *Am. J. Physiol. Heart Circ. Physiol.* **293**, H875 (2007).
 [3] F. Qu, C. M. Ripplinger, V. P. Nikolski, C. Grimm, and I. R. Efimov, *J. Biomed. Opt.* **12**, 044019 (2007).
 [4] E. M. Cherry and F. H. Fenton, *New J. Phys.* **10**, 125016 (2008).
 [5] A. Karma, *Chaos* **4**, 461 (1994).
 [6] M. Courtemanche and A. T. Winfree, *Int. J. Bifurcation Chaos Appl. Sci. Eng.* **1**, 431 (1991).
 [7] F. H. Samie and J. Jalife, *Cardiovasc. Res.* **50**, 242 (2001).
 [8] A. V. Panfilov, *Phys. Rev. Lett.* **88**, 118101 (2002).
 [9] F. H. Fenton, E. M. Cherry, H. M. Hastings, and S. J. Evans, *Chaos* **12**, 852 (2002).
 [10] J. Jalife, *Annu. Rev. Physiol.* **62**, 25 (2000).
 [11] J. M. Rogers and R. E. Ideker, *Circ. Res.* **86**, 369 (2000).
 [12] T. J. Wu, S. F. Lin, J. N. Weiss, C. T. Ting, and P.-S. Chen, *Circulation* **106**, 1859 (2002).
 [13] S. Nattel, *J. Cardiovasc. Pharmacol. Ther.* **8**, S5 (2003).
 [14] R. E. Ideker and J. M. Rogers, *Circulation* **114**, 530 (2006).
 [15] J. B. Nolasco and R. W. Dahlen, *J. Appl. Physiol.* **25**, 191 (1968).
 [16] M. R. Guevara, G. Ward, A. Shrier, and L. Glass, in *Computers in Cardiology 1984* (IEEE Computer Society, Long Beach, CA, 1984), p. 167.
 [17] J. M. Pastore, S. D. Girouard, K. R. Laurita, F. G. Akar, and D. S. Rosenbaum, *Circulation* **99**, 1385 (1999).
 [18] Z.-L. Qu, A. Garfinkel, P.-S. Chen, and J. N. Weiss, *Circulation* **102**, 1664 (2000).
 [19] T. Watanabe, F. Fenton, S. Evans, H. Hastings, and A. Karma, *J. Cardiovasc. Electrophysiol.* **12**, 196 (2001).
 [20] J. J. Fox, M. L. Riccio, F. Hua, E. Bodenschatz, and R. F. Gilmour, Jr., *Circ. Res.* **90**, 289 (2002).
 [21] B. R. Choi, W.-C. Jang, and G. Salama, *Heart Rhythm* **4**, 1057 (2007).
 [22] R. C. Myles, F. L. Burton, S. M. Cobbe, and G. L. Smith, *J. Mol. Cell. Cardiol.* **45**, 1 (2008).
 [23] D. S. Rosenbaum, L. E. Jackson, J. M. Smith, H. Garam, J. N. Ruskin, and R. J. Cohen, *N. Engl. J. Med.* **330**, 235 (1994).
 [24] M. L. Walker and D. S. Rosenbaum, *Cardiovasc. Res.* **57**, 599 (2003).
 [25] W. J. Rappel, F. Fenton, and A. Karma, *Phys. Rev. Lett.* **83**, 456 (1999).
 [26] B. Echebarria and A. Karma, *Chaos* **12**, 923 (2002).
 [27] D. J. Christini, M. L. Riccio, C. A. Cuiianu, J. J. Fox, A. Karma, and R. F. Gilmour, Jr., *Phys. Rev. Lett.* **96**, 104101 (2006).
 [28] M. Li and N. F. Otani, *Ann. Biomed. Eng.* **32**, 784 (2004).
 [29] D. Allexandre and N. F. Otani, *Phys. Rev. E* **70**, 061903 (2004).
 [30] S. Dubljevic, *Int. J. Robust Nonlinear Control* **19**, 135 (2009).
 [31] S. Dubljevic, S.-F. Lin, and P. D. Christofides, *Comput. Chem. Eng.* **32**, 2086 (2008).
 [32] B. Echebarria and A. Karma, *Phys. Rev. Lett.* **88**, 208101 (2002).
 [33] M. L. Koller, M. L. Riccio, and R. F. Gilmour, Jr., *Am. J. Physiol. Heart Circ. Physiol.* **275**, H1635 (1998).
 [34] G. Dominguez and H. A. Fozzard, *Am. J. Physiol.* **237**, C119 (1979).
 [35] P. Dorato, C. Abdallah, and V. Cerone, *Linear-Quadratic Control: An Introduction* (Prentice Hall, Englewood Cliffs, NJ, 1995).
 [36] B. D. O. Anderson and J. B. Moore, *Optimal Control: Linear Quadratic Methods* (Prentice Hall, Englewood Cliffs, NJ, 1990).
 [37] F. Fenton and A. Karma, *Chaos* **8**, 20 (1998).
 [38] A. Bueno-Orovio, E. M. Cherry, and F. H. Fenton, *J. Theor.*

- Biol. **253**, 544 (2008).
- [39] F. Fenton and A. Karma, *Chaos* **8**, 879 (1998).
- [40] M. Courtemanche, L. Glass, and J. P. Keener, *Phys. Rev. Lett.* **70**, 2182 (1993).
- [41] P. Comtois and A. Vinet, *Chaos* **17**, 023125 (2007).
- [42] Y. Lan and P. Cvitanović, *Phys. Rev. E* **69**, 016217 (2004).
- [43] E. G. Tolkacheva, D. G. Schaeffer, D. J. Gauthier, and C. C. Mitchell, *Chaos* **12**, 1034 (2002).
- [44] V. Jacquemet, *Math. Biosci.* **208**, 241 (2007).
- [45] R. B. Lehoucq, D. Sorensen, and C. Yang, *ARPACK Users' Guide: Solution of Large-Scale Eigenvalue Problems with Implicitly Restarted Arnoldi Methods* (SIAM Publications, Philadelphia, 1998).
- [46] N. F. Otani and R. F. Gilmour, Jr., *J. Theor. Biol.* **187**, 409 (1997).
- [47] S. M. Narayan and J. M. Smith, *J. Am. Coll. Cardiol.* **35**, 1485 (2000).
- [48] R. A. Horn and C. R. Johnson, *Matrix Analysis* (Cambridge University Press, Cambridge, N.Y., 1985).
- [49] T. Kailath, *Linear Systems* (Prentice Hall, Englewood Cliffs, N.J., 1980).
- [50] J. Stoer and R. Bulirsch, *Introduction to Numerical Analysis* (Springer-Verlag, New York, 1998).
- [51] G. Hagen and I. Mezić, *Proceedings of the 2000 American Control Conference*, Vol. 6 (American Automatic Control Council, New York, 2000), pp. 3783–3787.
- [52] A. Al-Khadra, V. Nikolski, and I. R. Efimov, *Circ. Res.* **87**, 797 (2000).
- [53] V. P. Nikolski and I. R. Efimov, *Europace* **7**, S146 (2005).
- [54] H. Tachibana, I. Kubota, M. Yamaki, T. Watanabe, and H. Tomoike, *Am. J. Physiol. Heart Circ. Physiol.* **275**, H116 (1998).
- [55] R. Grigoriev, *Physica D* **140**, 171 (2000).